ARTICLE TYPE

The Impact of Silicon Solar Cell Architecture and Cell Interconnection on Energy Yield in Hot & Sunny Climates[†]

Jan Haschke,*[a] Johannes P. Seif,[a] Yannick Riesen,[a] Andrea Tomasi,[a] Jean Cattin,[a] Loïc Tous,[b] Patrick Choulat,[b] Monica Aleman,[b] Emanuele Cornagliotti,[b] Angel Uruena,[b] Richard Russell,[b] Filip Duerinckx,[b] Jonathan Champliaud,[c] Jacques Levrat,[c] Amir A. Abdallah,[d] Brahim Aïssa,[d] Nouar Tabet,[d] Nicolas Wyrsch,[a] Matthieu Despeisse,[c] Jozef Szlufcik,[b] Stefaan De Wolf,[a,‡] Christophe Ballif[a,c]

Extensive knowledge of the dependence of solar cell and module performance on temperature and irradiance is essential for their optimal application in the field. Here we study such dependencies in the most common high-efficiency silicon solar cell architectures, including so-called Aluminum back-surface-field (BSF), passivated emitter and rear cell (PERC), passivated emitter rear totally diffused (PERT), and silicon heterojunction (SHJ) solar cells. We compare measured temperature coefficients (TC) of the different electrical parameters with values collected from commercial module data sheets. While similar TC values of the open-circuit voltage and the short circuit current density are obtained for cells and modules of a given technology, we systematically find that the TC under maximum power-point (MPP) conditions is lower in the modules. We attribute this discrepancy to additional series resistance in the modules from solar cell interconnections. This detrimental effect can be reduced by using a cell design that exhibits a high characteristic load resistance (defined by its voltage-over-current ratio at MPP), such as the SHJ architecture. We calculate the energy yield for moderate and hot climate conditions for each cell architecture, taking into account ohmic cell-to-module losses caused by cell interconnections. Our calculations allow us to conclude that maximizing energy production in hot and sunny environments requires not only a high open-circuit voltage, but also a minimal series-to-load-resistance ratio.

BROADER CONTEXT

In many developing countries, electricity is currently provided mostly by fossil fuel combustion. With ongoing industrial development and population growth in these countries, the demand for electricity will increase dramatically in the future. This electricity should be supplied by a cost-effective technology that is, in view of the Paris Agreement at the United Nations Framework Convention on Climate Change in 2015, based on renewable energy resources.

Silicon solar cells are perfectly suited to supply electricity under these conditions because the technology is mature and the base material is abundant. Furthermore, prices for solar cells have markedly decreased in recent years. Studies now indicate that solar will be the cheapest source of electricity in terms of capital expenditure, by 2030.

Understanding how different photovoltaic technologies are influenced by temperature is mandatory in selecting the best technology. We compare the temperature and irradiance dependencies of the current standard cell technology (silicon-based aluminum back surface field, BSF) with those of an emerging technology (passivated emitter rear cell, PERC) and other advanced

[a] Ecole Polytechnique Fédérale de Lausanne, Institute of Microengineering (IMT), Photovoltaics and Thin-Film Electronics Laboratory (PV-lab), Rue de la Maladière 71B, CH-2002 Neuchâtel, Switzerland. Fax: +41 21 695 42 01; Tel: +41 21 69 54384; E-mail: jan.haschke@epfl.ch

[b] Interuniversity Microelectronics Center (imec), Kapeldreef 75, BE-3001 Leuven, Belgium.

[c] Swiss Center for Electronics and Microtechnology (CSEM), PV-center, Rue Jaquet Droz 1, CH-2002 Neuchâtel, Switzerland.

[d] Qatar Environment and Energy Research Institute (QEERI), Hamad bin Khalifa University, Qatar Foundation, P.O. Box 5825, Doha, Qatar.

[‡] Present address: King Abdullah University of Science and Technology (KAUST), KAUST Solar Center (KSC), Thuwal, 23955-6900, Saudi Arabia

[†] Electronic Supplementary Information (ESI) available: [details of any supplementary information available should be included here]. See DOI: 10.1039/b000000x/

technologies such as silicon heterojunction solar cells. In addition, we discuss electrical cell-to-module losses and their impact on the energy production of each technology.

1 Introduction

To abide by the 2015 Paris Agreement of the United Nations Framework Convention on Climate Change, future energy production will have to be fully supplied by renewable energy resources[1]. Combined with storage solutions[2,3], a highly suitable candidate to produce 100 % CO_2-neutral energy is silicon photovoltaics (PV)[4,5]. Silicon PV is currently the dominant and most mature technology[7], and its base material is abundant, non-toxic and stable[8–10], making it also promising for terawatt deployment scenarios, provided a sufficiently low energy payback time can be guaranteed[6]. Furthermore, prices for silicon PV have dramatically decreased in recent years and current studies indicate that by 2030, PV will be the cheapest source of electricity in terms of capital expenditure in many regions of the world[11–13]. PV is already considered to be the most economical source of electricity in many regions in sub-Saharan Africa[14]. Recently, the lowest ever bids for solar parks were submitted at levelized cost of electricity (LCOE) between 0.0507 USD/kWh and 0.0242 USD/kWh[15–17]. The targeted capacities of these solar parks are in the range of hundreds of MW peak power, with optional future increases up to 5 GW[18]. They are located in hot and sunny climates (Abu Dhabi, Dubai, Mexico). Given the future demand for electricity in developing countries, we need clear understanding of the temperature-dependent performance of different photovoltaic technologies to accurately predict local LCOEs, especially when considering that accurate LCOE prediction in general is a very challenging task[19].

It is an established fact that the output power of silicon-based photovoltaic devices usually decreases with increasing temperature. These effects have been studied extensively in the past[20–22], most commonly observed is the reduced open-circuit voltage (V_{OC}) at higher temperatures, which is driven by increased intrinsic carrier density and thus increased recombination current in the absorber material. Because it is directly linked to the operating voltage[23,24], the fill factor (FF) usually also decreases with increased temperature. The short-circuit current density (J_{SC}) increases on the contrary because of temperature-triggered reduction of the absorber bandgap[22]. Other secondary phenomena may also affect the relationship between temperature and device performance, such as the presence of carrier transport barriers inside the electrical contacts[25–28] and temperature-dependent minority charge carrier recombination in the bulk and at the surfaces of the absorber[29–31].

In this paper, we analyze state-of-the-art solar cell architectures based on p-type and n-type crystalline silicon, including the current industrial standard solar cell technology (i.e. aluminum back surface field, BSF) as well as other more advanced technologies, including passivated emitter and rear contact[32] (PERC), passivated emitter rear totally diffused[33] (PERT), and silicon heterojunction[34] (SHJ) solar cells, which are expected to have increased industrial importance in the near future[35]. In addition to temperature- and irradiance-dependent current-voltage $J(V)$
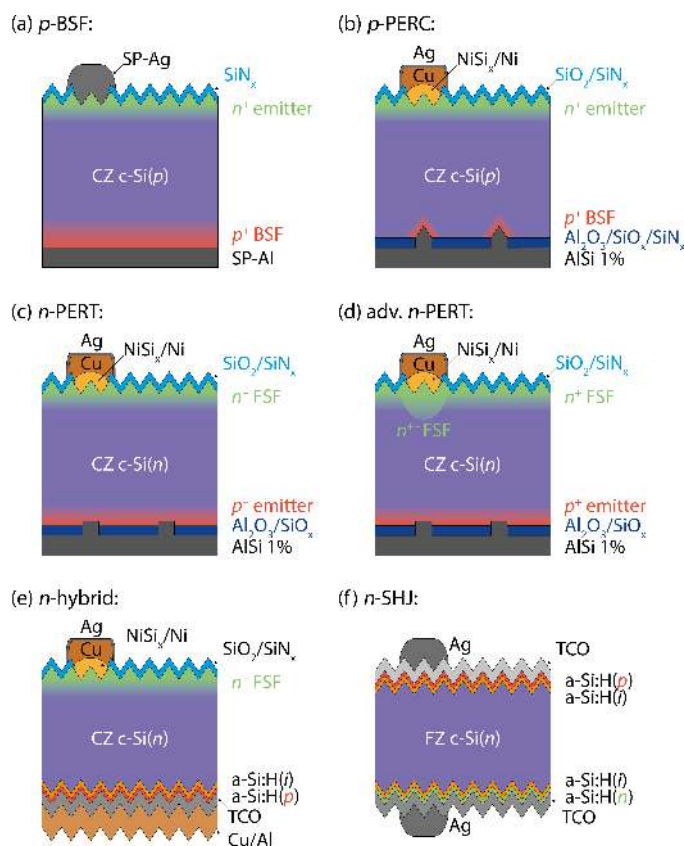
Fig. 1 Schematic sketches of the different device architectures investigated in this study.

measurements, we also examine the influence that operating temperature has on the surface passivation schemes used in the different cell architectures by measuring temperature-dependent transient photoconductance decay[30,36]. Furthermore, we examine the impact of ohmic cell-to-module losses that occur due to the series resistance associated with cell interconnections, and how these losses impact TC and energy generation of each architecture in hot and moderate climates.

2 Experimental

2.1 Device architectures

The different solar cell architectures examined in this paper are shown in Fig.1. Here we present a brief overview of device fabrication. More details as well as the extracted current-voltage ($J(V)$) parameters under standard test conditions (STC) are given in Table 1 and in the references provided hereafter. Two devices based on p-type c-Si are examined: BSF[37] and PERC[38].

The p-BSF cell features a diffused n^+ electron contact at the front, which is passivated by a silicon nitride (SiN_x) anti-reflection coating (ARC), a screen-printed (SP) front contact silver grid and a full-area SP aluminum BSF as the hole contact.

The p-PERC cell also has a diffused n^+ electron contact at the front, which is passivated by an SiO_2/SiN_x ARC stack. The front contact grid is electroplated and consists of a stack of nickel, copper and silver. On the rear side, the $Al_2O_3/SiO_x/SiN_x$ passivation and rear reflector stack is locally opened with a laser and subse-

Table 1 Data corresponding to the samples of Fig. 1, including the $J(V)$ parameters at standard test conditions (STC, 25 °C, AM1.5g spectrum, 1000 W m^{-2}). As for the type of the wafer the italic letter (p or n) stands for the doping type, and Cz for the crystal growth process (Czochralski). ρ stands for the resistivity of the wafer. R_{MPP} is the characteristic load resistance at maximum power conditions ($R_{MPP}=V_{MPP}/J_{MPP}$), η stands for the power conversion efficiency

| architecture | wafer | | | | $J(V)$ parameter at STC | | | | |
| | type | thickness | ρ | size | V_{OC} | J_{SC} | FF | R_{MPP} | η |
		(μm)	(Ω cm)	(cm^2)	(mV)	(mA cm^{-2})	(%)	(Ω cm^2)	(%)
p-BSF	p-Cz	170	1.5	238.95	640	37.0	78.6	15.4	18.6
p-PERC	p-Cz	170	1.5	238.95	655	38.7	79.3	15.2	20.0
n-PERT	n-Cz	160	4.0	227.06	677	39.3	81.3	15.5	21.6
adv. n-PERT	n-Cz	160	4.0	227.06	687	39.4	80.7	15.6	21.8
n-hybrid	n-Cz	180	4.0	227.06	678	38.3	79.8	15.8	20.8
n-SHJ	n-Cz	180	1.5	243.36	733	37.4	78.4	17.6	21.5

quently covered with sputtered AlSi1% (aluminum with 1 % silicon), and finally annealed to form a localized hole contact in the ablated areas[38].

All other devices are based on n-type c-Si. The standard and "advanced" passivated emitter, rear totally-diffused cells[39–41], n-PERT and adv. n-PERT, respectively, feature a full-area p$^+$ hole contact on the rear side, locally contacted through laser-ablated vias in an Al$_2$O$_3$/SiO$_x$ passivation and rear reflector layer stack by sputtered AlSi1%. Both variants feature a full-area diffused n$^+$ front-surface field (FSF) and a plated Ni/Cu/Ag front contact grid, as well as an SiO$_2$/SiN$_x$ AR and passivation stack. What differentiates the adv. n-PERT cell from the standard one is an additional local n^{++} region below the front contact grid that is obtained by laser doping to reduce contact recombination.

The n-hybrid cell[42] has the same front side as the n-PERT cell, but the rear contact is a so-called passivating contact, realized by silicon heterojunction technology. The contact consists of an intrinsic and a p-type amorphous silicon layer (a-Si:H(i) and a-Si:H(p), respectively), giving it hole-collecting properties, capped by a stack of a transparent conductive oxide (TCO) and Cu/Al metallization.

The full SHJ solar cell[34,43] (n-SHJ) features passivating contacts of both carrier types, formed by a-Si:H(i)/a-Si:H(p) and a-Si:H(i)/a-Si:H(n) stacks on the front and rear side, respectively. The a-Si:H layers on both sides are covered with TCO and a SP silver grid. The p-BSF and the n-SHJ cells were provided by external suppliers.

Furthermore, symmetrical test samples, featuring the same passivating schemes as used in the cells were prepared to test the temperature dependency of the passivation of each surface. In the solar cells featuring direct metal contacts, the symmetrical samples thus only represent the passivated areas.

We note that the performance of the analysed cells (Table 1) is representative of both the performance currently achieved in commercially available modules with the same cell architecture, and cells fabricated with our manufacturing process. The device-to-device variability for the silicon solar cells listed in Table 1 is below 0.3 %$_{abs}$[38,44,45].

2.2 Characterisation / Methodology

2.2.1 Temperature- and irradiance-dependent *J(V)*.

The cells were measured with a $J(V)$ probing station (AM1.5g, class A$^+$A$^+$A$^+$ sun simulator with a temperature-controllable chuck). The temperature was varied between 15 °C and 75 °C, and the irradiation intensity was varied between 0.036 to 2 suns by the application of different neutral density filters or lenses. We obtained a matrix of the irradiance- and temperature-dependent power output of each solar cell.

To accurately determine TCs of the $J(V)$ parameters, the correct identification of the (relative) temperature is mandatory. We therefore took several measures to ensure that the cell temperature during the measurement was the same under V_{OC}, J_{SC}, and maximum-power-point (MPP) conditions, and that the surface temperature of the chuck was accurately known (see supplementary information). To obtain the relative TCs, we linearly fitted the data between 25 °C and 75 °C and normalised to the value at 25 °C, as follows:

$$\underbrace{\frac{1}{P_{MPP}^{25\,°C}}\frac{dP_{MPP}}{dT}}_{TC_{P_{MPP}}} = \underbrace{\frac{1}{V_{OC}^{25\,°C}}\frac{dV_{OC}}{dT}}_{TC_{V_{OC}}} + \underbrace{\frac{1}{J_{SC}^{25\,°C}}\frac{dJ_{SC}}{dT}}_{TC_{J_{SC}}} + \underbrace{\frac{1}{FF^{25\,°C}}\frac{dFF}{dT}}_{TC_{FF}}, \quad (1)$$

where $P_{MPP}^{25\,°C}$, $V_{OC}^{25\,°C}$, $J_{SC}^{25\,°C}$ and $FF^{25\,°C}$ are the values of the repective quantities at 25 °C. If not stated otherwise, all TCs given in the paper are relative TCs (normalized to the respective value at 25 °C).

2.2.2 Temperature-dependent charge carrier lifetime.

To determine the temperature-dependent minority charge carrier lifetime, we used a Sinton Instruments WCT-120TS[46], and followed the generalized analysis method[47]. The injection-dependent lifetime of the symmetrical samples capturing either the front or the rear side of the devices was measured at different temperatures between 30 °C and 120 °C. To avoid any effect induced by annealing during the measurement itself, the symmetrical samples were annealed prior to the measurements for 20 min at 190 °C. Furthermore, a reference lifetime measurement was performed before and after the temperature-dependent measurements to ensure that the characteristics of the samples did not change during the measurement. For the actual measurement,

the chuck of the WCT-120TS was heated to 125 °C and a sample was placed on the chuck. Then, the measurements were performed while the chuck and sample were passively cooling down.

2.2.3 Calculation of annual energy production.

To calculate annual energy production at two locations (Geneva and Abu Dhabi), we used weather data provided by the American Society of Heating, Refrigerating and Air-Conditioning Engineers (ASHRAE)[48]. The data describe a typical meteorological year and include irradiance data, as well as air temperature and wind speed at the given location in hourly timesteps. First, the effective in-plane irradiance and the module temperature were calculated based on the weather data and the PV-lib toolbox*[49]. The module plane was tilted south by 40° for Geneva, and by 30° for Abu Dhabi, as these angles lead to the highest annual energy production at the respective locations, corresponding to their latitudes.

In addition to the temperature- and irradiance-dependent power output for each solar cell, obtained as described in section 2.2.1, the produced energy per time step was then calculated. When ohmic cell-to-module losses were included, the power was calculated using equation (7). More details are given in the supplementary information.

3 Results and discussion

3.1 Temperature-dependent charge carrier lifetime

In Fig. 2, the injection-dependent carrier lifetimes for symmetrical samples representative of the passivation in p-PERC, n-PERT and n-SHJ solar cells are shown for temperatures between 30 °C and 120 °C. An increase in the minority carrier lifetime with increasing temperature is observed in all passivation schemes investigated here.

As the temperature dependency of both Auger and radiative recombination in a silicon wafer is negligible in the investigated temperature range[50–52], changes in the minority carrier lifetime most likely arise from the temperature dependency of Shockley-Read-Hall (SRH) recombination statistics in the bulk or at the surfaces. An increase in lifetimes of passivated[29] and unpassivated[30] silicon bulk material has been reported in the literature. Schmidt attributed the lifetime increase to the temperature dependent decrease of the hole capture cross section of Al-related defects in the silicon bulk material[29].

The temperature-dependent lifetime of silicon heterojunction passivating contacts was studied by Seif *et al.*[31]. They reported an increase in the carrier lifetime with a-Si:H(i/p) and a-Si:H(i/n) passivating layers, but a decrease in carrier lifetime with a-Si:H(i) passivation. The origin of the increasing charge carrier lifetime in silicon is not fully understood yet. However, the findings underscore that the temperature dependency of the minority carrier lifetime can influence the TC of the V_{OC} and therefore has to be considered for accurate modelling, as further discussed in Section 3.3.
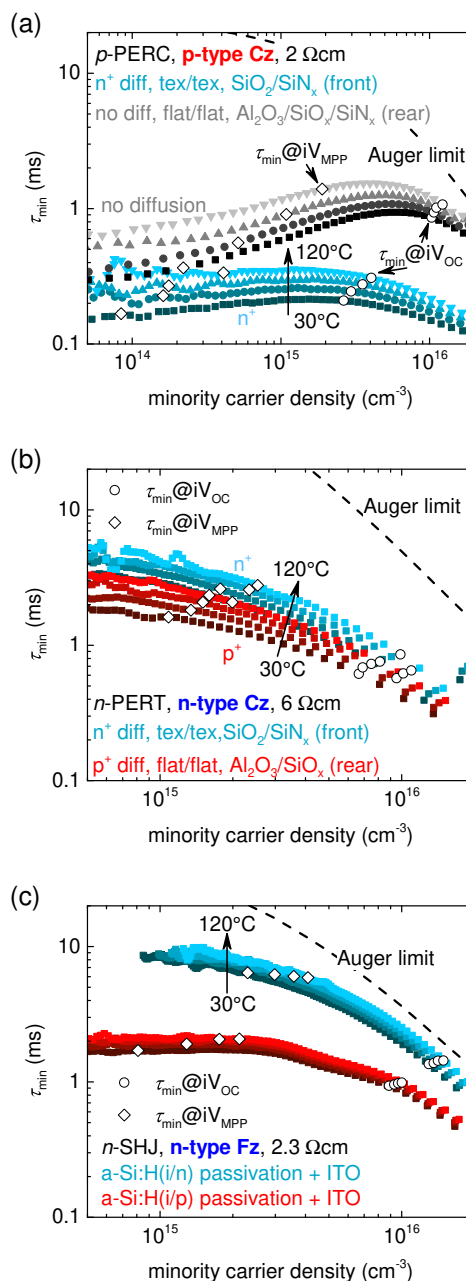
Fig. 2 Injection-dependent effective minority carrier lifetime, τ_{min}, of symmetrically passivated samples as obtained from temperature-dependent minority carrier lifetime measurements on a Sinton WCT-120TS setup. The lifetime curves indicate the passivation schemes in the investigated cells. (a) on p-type c-Si, homojunction passivation, (b) on n-type c-Si (homojunction), (c) on n-type c-Si (a-Si:H(i/p) and a-Si:H(i/n) passivation).
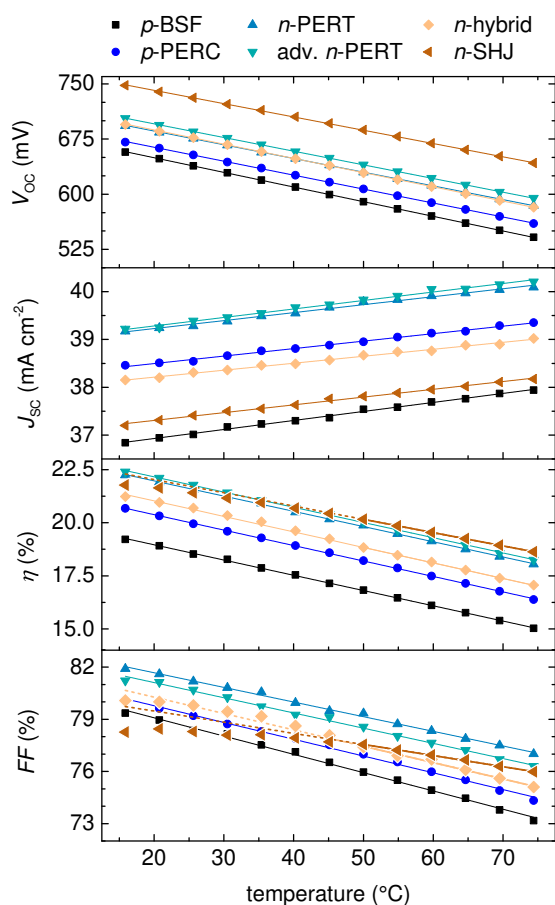
Fig. 3 Temperature-dependent $J(V)$ parameters of the investigated solar cell architectures. The measurements were taken under AM1.5g irradiance at $1000\,\mathrm{W\,m^{-2}}$. The parameters depend linearly on the temperature except for the FF of the solar cells incorporating silicon heterojunctions. As a consequence also the temperature dependency of the efficiency η is non-linear for these devices. The data were linearly least-square fitted to derive the TCs, as indicated by the solid lines. Dashed lines indicate linear extrapolation.

3.2 Temperature coefficients of *J(V)* parameters

In Fig. 3, the temperature-dependent $J(V)$ parameters of all investigated device architectures are shown at standard $1000\,\mathrm{W\,m^{-2}}$, with AM1.5g irradiation. It can be seen that in general the parameters of the cells linearly follow the temperature. However, for FF and, as a consequence, also for the efficiency, η, this is not the case in the two cell architectures incorporating a silicon heterojunction passivating contact. The effect is more pronounced for the n-SHJ cell compared with the n-hybrid cell. The non-linearity of FF and η versus temperature was previously observed in such contacts [25,28,53] and is commonly observed in solar cells incorporating thermionic barriers. Generally, increasingly linear behaviour can be achieved by increasing the conductivity of the contact layer [28] and the use of thinner intrinsic buffer layers [25], for which the challenge is to maintain sufficient surface passivation.

Due to the non-linearity of the cells investigated here, the linear fitting to obtain the TCs was limited to the range between $50\,^{\circ}\mathrm{C}$ and $75\,^{\circ}\mathrm{C}$ in the n-hybrid and n-SHJ cells. In Table 2, the relative TCs of the investigated cells are summarized. The values obtained

Table 2 Relative TCs at AM1.5g irradiance of $1000\,\mathrm{W\,m^{-2}}$ of the devices shown in Fig. 1, derived from linear fitting between $25\,^{\circ}\mathrm{C}$ and $75\,^{\circ}\mathrm{C}$ of the temperature-dependant $J(V)$ parameters shown in Fig. 3. For the TCs marked with an asterisk, the fitting was limited to the range between $50\,^{\circ}\mathrm{C}$ and $75\,^{\circ}\mathrm{C}$, as the data are only linear in this range. To obtain the relative TCs in these cases, $P_{\mathrm{MPP}}^{25\,^{\circ}\mathrm{C}}$, $FF^{25\,^{\circ}\mathrm{C}}$ and $R_{\mathrm{MPP}}^{25\,^{\circ}\mathrm{C}}$ were obtained by linear extrapolation. Fitting between $25\,^{\circ}\mathrm{C}$ and $75\,^{\circ}\mathrm{C}$ would lead to a TC_{FF} of $-0.05\,\%\,\mathrm{K^{-1}}$ and thus $\mathrm{TC}_{P_{\mathrm{MPP}}}$ of $-0.26\,\%\,\mathrm{K^{-1}}$ for the n-SHJ solar cell. Additionally, the temperature coefficient of the characteristic load resistance, $\mathrm{TC}_{R_{\mathrm{MPP}}}$, is included.

architecture	$\mathrm{TC}_{V_{\mathrm{OC}}}$ (%/K)	$\mathrm{TC}_{J_{\mathrm{SC}}}$ (%/K)	TC_{FF} (%/K)	$\mathrm{TC}_{P_{\mathrm{MPP}}}$ (%/K)	$\mathrm{TC}_{R_{\mathrm{MPP}}}$ (%/K)
p-BSF	-0.31	0.05	-0.14	-0.39	-0.39
p-PERC	-0.29	0.04	-0.12	-0.36	-0.37
n-PERT	-0.28	0.04	-0.11	-0.33	-0.34
adv. n-PERT	-0.27	0.04	-0.11	-0.33	-0.33
n-hybrid	-0.28	0.04	-0.12*	-0.35*	-0.33*
n-SHJ	-0.25	0.04	-0.08*	-0.29*	-0.30*

from the limited fitting range are marked with an asterisk. Relative TCs were normalized to the value at $25\,^{\circ}\mathrm{C}$. We maintained this normalization for the two non-linear cases. However, to preserve comparability with the TCs of the other architectures, $P_{\mathrm{MPP}}^{25\,^{\circ}\mathrm{C}}$ and $FF^{25\,^{\circ}\mathrm{C}}$ (cf. equation (1)) were not taken from Table 1, but instead calculated by linear extrapolation using the fitted TC[†]. The $\mathrm{TC}_{J_{\mathrm{SC}}}$ is similar for all investigated cells and positive. The J_{SC} increases with temperature due to the reduced band-gap of silicon at higher temperatures [22] and the accompanied enhanced absorption of infrared wavelengths [54].

The cell architecture with the highest (best) $\mathrm{TC}_{P_{\mathrm{MPP}}}$ is the n-SHJ architecture. This is due to higher $\mathrm{TC}_{V_{\mathrm{OC}}}$ and TC_{FF}. Included in Table 2 is also the TC of the characteristic load resistance at MPP ($\mathrm{TC}_{R_{\mathrm{MPP}}}$). For $\mathrm{TC}_{R_{\mathrm{MPP}}}$ the value of the n-SHJ cell is the most favourable. Maintaining a higher characteristic resistance at MPP with increasing temperature helps to avoid the detrimental influence of series resistance caused by the interconnection of the cells in a module. This is discussed in Section 3.4.

3.3 Comparison of V_{OC} versus temperature with models from the literature.

In Fig. 4, the relationships between the open-circuit voltage and temperature in four of the cell architectures, p-BSF, p-PERC, advanced n-PERT and n-SHJ are compared; the others are not shown for clarity. We also show the same relationships as determined by two models in the literature. The first model was proposed by Green *et al.* [20,55] and describes the absolute $\mathrm{TC}_{V_{\mathrm{OC}}}$ ($\mathrm{TC}_{V_{\mathrm{OC}}}^{\mathrm{abs}}$) as a function of the V_{OC} at $25\,^{\circ}\mathrm{C}$:

$$\mathrm{TC}_{V_{\mathrm{OC}}}^{\mathrm{abs}} = -\frac{\frac{E_{g0}^{\mathrm{Si}}}{q} - V_{\mathrm{OC}}^{25\,^{\circ}\mathrm{C}} + \gamma \cdot kT}{T}, \qquad (2)$$

[†] The values for $P_{\mathrm{MPP}}^{25\,^{\circ}\mathrm{C}}$ and $FF^{25\,^{\circ}\mathrm{C}}$ obtained in this way are higher than the measured values of the cells. They correspond to the hypothetical values that the cells would exhibit without non-linear transport barriers.
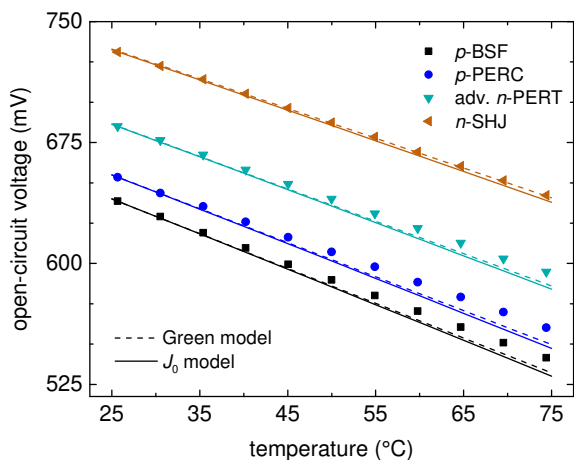
Fig. 4 V_{OC} values of four of the investigated solar cells versus temperature compared with two different modelled characteristics: a formula for the $TC_{V_{OC}}$ as proposed by Green *et al.*[20,55] and $V_{OC}(T)$ calculated from the temperature dependency of J_0 due to SRH recombination at low injection[57].

Fig. 5 Schematic circuit of the solar cell and the additional resistance caused by the cell interconnection/wiring R_{CTM}. The detrimental influence of R_{CTM} is less when R_{MPP} is large.

with the absolute temperature, T = 298.15 K, the bandgap of silicon at 0 K divided by the elementary charge $E_{g0}^{Si}/q = 1.206$ V, the Boltzmann constant, $k = 8.617$ V K^{-1}, and a factor depending on the mechanism determining the open-circuit voltage[55] $\gamma = 3$.

In the second model, the temperature dependency of the recombination parameter, J_0, of the classical one-diode model is used to calculate $V_{OC}(T)$ with equations (3) and (4), taking $J_{SC}(T)$ from the measured data (see Fig 3).

$$V_{OC}(T) = \ln\left(\frac{J_{SC}(T)}{J_0(T)}\right) \tag{3}$$

When assuming a constant minority carrier lifetime, τ_{min}, the temperature dependence of the recombination parameter, J_0, stems only from the temperature dependence of the intrinsic carrier concentration, n_i, described by the model of Misiakos and Tsamakis[56], which was used for the calculations presented here. With this, $J_0(T)$ is described as[57]

$$J_0(T) = q\frac{n_i^2(T) \cdot W}{N_{dop} \cdot \tau_{min}} \tag{4}$$

with the elementary charge, q, the wafer thickness, W, the doping concentration of the majority charge carrier in the wafer, N_{dop}, and the minority charge carrier lifetime, τ_{min}. W was taken from Table 1, N_{dop} was calculated from the wafer's resistivity and τ_{min} was chosen such that the V_{OC} derived from the model matches the measured value (see Table 1) at 25 °C.

As can be seen from Fig. 4, both models deviate from the measured trends of $V_{OC}(T)$ for most of the cells, seen by an underestimation of the the V_{OC} at higher temperatures. The deviation is more pronounced in the cells with lower V_{OC} at 25 °C and almost vanishes in the n-SHJ cell, which features the highest V_{OC}, approaching the theoretical limit. It should be noted that equation (4) is only valid for so-called low injection conditions[57] (the minority carrier density is much lower than doping density). Strictly speaking, this is only true for the p-BSF and p-PERC cells, but not
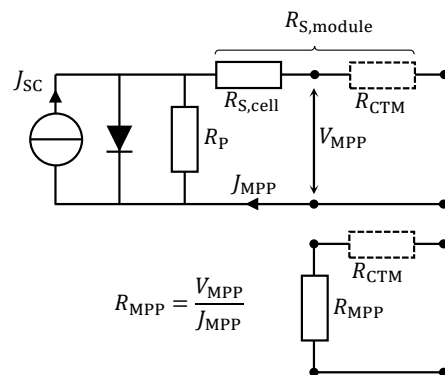
for the n-PERT and the n-SHJ cell. However, especially for the cells were the model should be valid, it deviates from the measured data. This can be explained by the increased minority carrier lifetime (τ_{min}) at higher temperatures, as reported in Section 3.1. As τ_{min} increases with increasing temperature, the decrease of the V_{OC} with increasing temperature is lowered, leading thus to a higher $TC_{V_{OC}}$ than predicted by the models. This is not the case for the n-SHJ solar cell, because V_{OC} is already close to the Auger limit and the temperature dependence of Auger recombination is negligible in the investigated temperature range[50].

3.4 From cell to module

When going from solar cells to solar modules, additional optical losses occur due to enhanced parasitic absorption and reflection caused by encapsulant and glass, and additional electrical losses occur due to cell interconnections. While the additional optical losses have no or only a minor impact, the additional electrical losses change the temperature dependency of the device, which we discuss here.

In Table 3, the specifications of commercial solar cell modules are given, taken from data sheets for p-BSF, p-PERC, adv. n-PERT and n-SHJ modules. While the relative TC of the V_{OC} and the J_{SC} are comparable with our data obtained from the individual cells, the TC_{FF} of the modules is generally lower. We find that this lower TC_{FF} comes from the additional series resistance, caused by cell interconnections, as a silicon solar cell with a lower FF due to a higher series resistance will have a worse TC_{FF}[21], which we elucidate in the following.

The power density generated by a solar cell that is delivered to the external circuit is

$$P_{MPP} = V_{MPP} \cdot J_{MPP} = J_{MPP}^2 \cdot R_{MPP} , \tag{5}$$

with the characteristic load resistance at MPP $R_{MPP} = V_{MPP}/J_{MPP}$. The power lost from an additional series resistance, R_{CTM}, can then be approximated by

$$P_{loss}^{CTM} \approx J_{MPP}^2 \cdot R_{CTM} . \tag{6}$$

This approximation is valid as long as J_{MPP} does not change with

| manufacturer, product	cell type	power (W)	V_{OC}/cell (mV)	FF_{module} (%)	η_{module} (%)	$TC_{J_{SC}}$ (%/K)	$TC_{V_{OC}}$ (%/K)	TC_{FF}* (%/K)	$TC_{P_{MPP}}$ (%/K)
SolarWorld, SW 320 XL mono	p-BSF	320	638	74.6	16.0	0.04	-0.30	-0.17	-0.43
Trina, ALLMAX PD05 265 (multi)	p-BSF	265	638	76.1	16.2	0.05	-0.32	-0.14	-0.41
SolarWorld, SW 270 mono	p-PERC	270	653	73.6	16.1	0.04	-0.30	-0.15	-0.41
Q CELLS, Q.PLUS-G4	p-PERC	280	653	74.9	16.8	0.04	-0.29	-0.15	-0.40
LG, NeON2 LG320N1C-G4	n-PERT	320	682	77.9	19.5	0.03	-0.28	-0.13	-0.38
Panasonic, VBHN330SA16	n-SHJ	330	726	78.1	19.7	0.03	-0.25	-0.08	-0.30

additional R_{CTM}, which is true for the cases considered here[‡]. In all silicon solar cell devices, R_{MPP} reduces when the temperature increases, as V_{MPP} drops, but J_{MPP} generally stays constant[§]. On the other hand, R_{CTM} will increase with increased temperature[¶]. P_{loss}^{CTM} also increases, while P_{MPP} decreases with increased temperature due to the reduction of V_{MPP}. Therefore, the fraction of power lost at R_{CTM} under MPP conditions increases with increased temperature. Since the temperature dependencies of both V_{OC} and J_{SC} are not affected by R_{CTM}, TC_{FF} is reduced .

The power at MPP including the reduction due to an additional R_{CTM} can be calculated using

$$P_{MPP}^{module} = P_{MPP}^{cell} \frac{R_{MPP}^{cell} - R_{CTM}}{R_{MPP}^{cell}}, \text{ with } R_{MPP}^{cell} = \frac{V_{MPP}^{cell}}{J_{MPP}^{cell}} . \qquad (7)$$

From this, it is evident that a device with a large R_{MPP} (larger V_{MPP} and lower or equal J_{MPP}) will generally be less sensitive to additional series resistance. To achieve higher performance at higher temperatures, it is thus important to maintain R_{MPP} as high as possible. Comparing the R_{MPP} of the different architectures (Table 1) with its temperature coefficient ($TC_{R_{MPP}}$, Table 2), suggests that n-SHJ is best suited for applications in hot climates, as both the R_{MPP} as well as its $TC_{R_{MPP}}$ are the highest values among the examined architectures.

In Fig. 6, the relative power output versus temperature of the p-BSF cell is shown, as well as the relative power trend of a corresponding module (SolarWorld SW 320 XL, $TC_{P_{MPP}}^{module} = 0.43\,\%\,\text{K}^{-1}$). Furthermore, relative power trends that were calculated from the cell data using equation (7) and an additional temperature-dependent $R_{CTM}(T)$ of $0.5\,\Omega\,\text{cm}^2$ and $1.0\,\Omega\,\text{cm}^2$ at $25\,°C$ ($R_{CTM}^{25\,°C}$) are shown. The temperature-coefficient of R_{CTM} ($TC_{R_{CTM}}$) was estimated from the literature[58] to amount to $-0.4\,\%\,\text{K}^{-1}$. It can be seen that the $TC_{P_{MPP}}$ deteriorates with the additional series resistance. As $TC_{V_{OC}}$ and $TC_{J_{SC}}$ are both not affected by a series resistance, this change is due to a decrease in TC_{FF}. In the case here, the trend calculated from the cell data assuming an $R_{CTM}^{25\,°C}$ of $0.8\,\Omega\,\text{cm}^2$ (data not shown in the
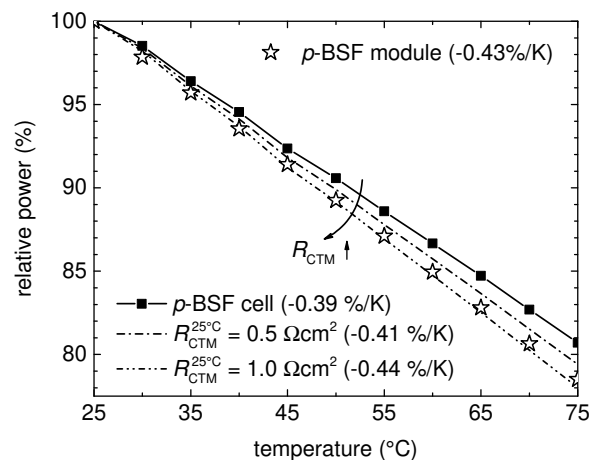
Fig. 6 Relative power (normalized to P_{MPP} at $25\,°C$) versus temperature for the p-BSF cell at $1000\,\text{W m}^{-2}$ with AM1.5g irradiation. The dash-dotted lines are calculated from the cell data using equation (7) for each temperature step and assuming an additional temperature-dependent ($TC_{R_{CTM}} = -0.4\,\%\,\text{K}^{-1}$) series resistance, R_{CTM}, of $0.5\,\Omega\,\text{cm}^2$ and $1\,\Omega\,\text{cm}^2$ at $25\,°C$. The values in brackets correspond to $TC_{P_{MPP}}$ and were obtained by linear fitting. The relative power of the module is calculated with the $TC_{P_{MPP}}$ of the SolarWorld SW 320 XL module taken from Table 3.

figure) would fit well with the trend of the module ($TC_{P_{MPP}}^{module} = 0.43\,\%\,\text{K}^{-1}$). This can only be taken as an approximate value. For accurate determination of R_{CTM}, data on the cells in the module are necessary. For example, the cells in the Panasonic module probably feature a higher FF than the n-SHJ cell considered in our study, as the difference in FF between our cell and the module data is only $0.2\,\%_{abs}$ (cf. Tables 1 and 3). Furthermore, another source of error in module data sheets is obvious: often, several $J(V)$ parameter data sets are given for different power classes but only one data set is provided for the TCs. To which $J(V)$ parameter data set it belongs is usually not stated. As the V_{OC} per cell changes up to $10\,\text{mV}$ between the different sets, this would obviously lead to different $TC_{V_{OC}}$.

Summing up, additional series resistance due to cell interconnections in a module leads to a lower TC_{FF} for the module than for single cells. Based on literature data[59,60], we assume $R_{CTM}^{25\,°C}$ is generally below $1.0\,\Omega\,\text{cm}^2$.

Under the aforementioned assumption that the change of J_{MPP} with increased temperature is negligible, and if $TC_{P_{MPP}}$ of a cell and its R_{MPP} at $25\,°C$ conditions are known, the TC of a corresponding module including a temperature-dependent R_{CTM} can

---

[‡] Using the one-diode-model for cells with $V_{OC} > 600\,\text{mV}$ and if $R_{CTM} < 2\,\Omega\,\text{cm}^2$, J_{MPP} changes only marginally.

[§] In the one-diode model without series resistance, J_{MPP} slightly increases with increasing temperature, as J_{SC} also increases. However, with additional R_S, J_{MPP} stays constant and even decreases with higher R_S. In the investigated solar cells, J_{MPP} is constant in the investigated temperature range (data not shown).

[¶] The specific resistance of a metal like copper generally increases with increased temperature[58]. In the literature, the relative $TC_{R_{CTM}}$ is normalized to $20\,°C$.

be calculated as

$$\text{TC}_{P_{\text{MPP}}}^{\text{module}} = \underbrace{\frac{R_{\text{MPP}}^{\text{cell,STC}}}{R_{\text{MPP}}^{\text{cell,STC}} - R_{\text{CTM}}^{25\,°C}} \cdot \text{TC}_{P_{\text{MPP}}}^{\text{cell}}}_{\text{impact of } R_{\text{CTM}}} - \underbrace{\frac{R_{\text{CTM}}^{25\,°C}}{R_{\text{MPP}}^{\text{cell,STC}} - R_{\text{CTM}}^{25\,°C}} \cdot \text{TC}_{R_{\text{CTM}}}}_{\text{impact of temp. dependence of } R_{\text{CTM}}} \, .$$

(8)

Equation (8) is derived in the supplementary information and highlights two main conclusions:

(i) a solar cell architecture featuring a high R_{MPP} will be less susceptible to power losses due to R_{CTM}. One such architecture is the SHJ architecture or, more generally, passivating contact architectures due to their high V_{OC}s,

(ii) ohmic losses (due to cell interconnections, R_{CTM}) should be as low as possible, especially in hot and sunny environments. $\text{TC}_{P_{\text{MPP}}}^{\text{module}}$ decreases with increasing R_{CTM}.

These findings are generally valid for silicon solar cells and not limited to a specific absorber material. The strategy to reduce ohmic losses on the module level using a high R_{MPP} (high voltage, low current) is also reflected in the approach of using half-cells for module fabrication[61]. However, this is only beneficial if the metallization of the cells is designed as if they were full-cells. General strategies to reduce the series resistance on modules but also on the cell level are reflected in multi-busbar and multi-wire interconnection technologies[62–64].

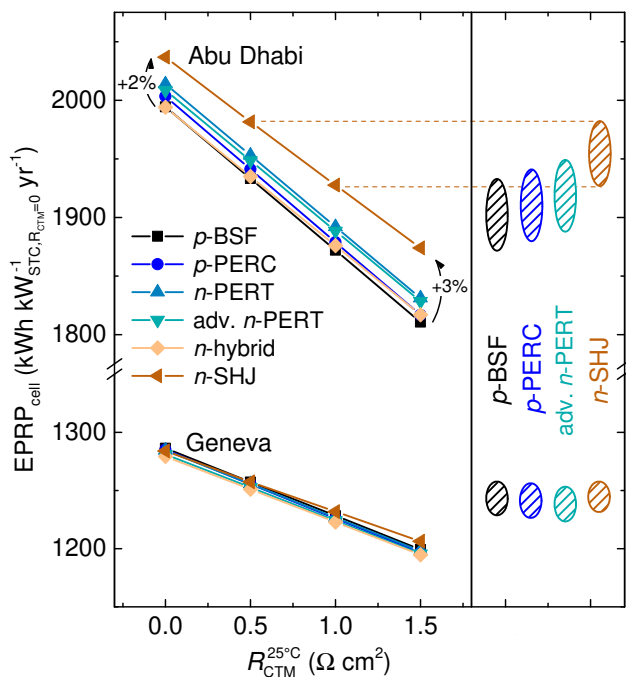### 3.5 Annual energy production

When comparing different photovoltaic systems with respect to their energy production performance, the energy per rated power under STC (yield)[||] in kWh/kW is usually used. In the case presented here, no solar *systems* are compared but single solar cells. Therefore, the most accurate performance measure would be the array yield, Y_A, as defined in IEC 61724[65] as

$$Y_A = \frac{E_{\text{yr}}}{P_{\text{MPP}}^{\text{STC}}} \, ,$$

(9)

with the produced energy per year and area (E_{yr}) and the rated power per area at STC ($P_{\text{MPP}}^{\text{STC}}$). However, using Y_A to compare different technologies can be misleading in this case here, as added R_{CTM} will lead to higher Y_A[67] (cf. supplementary information). That is because $P_{\text{MPP}}^{\text{STC}}$ is more strongly reduced by an additional R_{CTM} than E_{yr} as part of the energy is also produced at irradiance levels lower than STC, where R_{CTM} (or rather R_S in general) is less detrimental. Therefore, we divide the produced energy by the rated power *at the cell level*, i.e. STC and $R_{\text{CTM}} = 0\,\Omega\,\text{cm}^2$ ($P_{\text{MPP}}^{\text{STC,cell}}$) for each architecture and define the energy per rated power at the cell level as

$$\text{EPRP}_{\text{cell}} = \frac{E_{\text{yr}}}{P_{\text{MPP}}^{\text{STC,cell}}} \, .$$

(10)

In Fig. 7, the trends of $\text{EPRP}_{\text{cell}}$ are shown for the different solar

Fig. 7 Yearly energy production per rated power at cell level ($R_{\text{CTM}} = 0$, STC) for temperate (Geneva) and subtropical (Abu Dhabi) climate conditions. The data were calculated based on the temperature- and irradiance-dependent measurements of the different cell architectures and assuming temperature-dependent R_{CTM}. Lines are guides to the eye. The dashed areas on the right illustrate the trends for four architectures, assuming that $R_{\text{CTM}}^{25\,°C}$ is between $0.5\,\Omega\,\text{cm}^2$ and $1\,\Omega\,\text{cm}^2$ at the two different locations.

|| Unfortunately, the term yield is often used in an ambiguous manner. The annual energy production of a solar system is often referred to as yield. However, we abide by the terminology provided by the international standard IEC 61724[65,66] to avoid confusion.
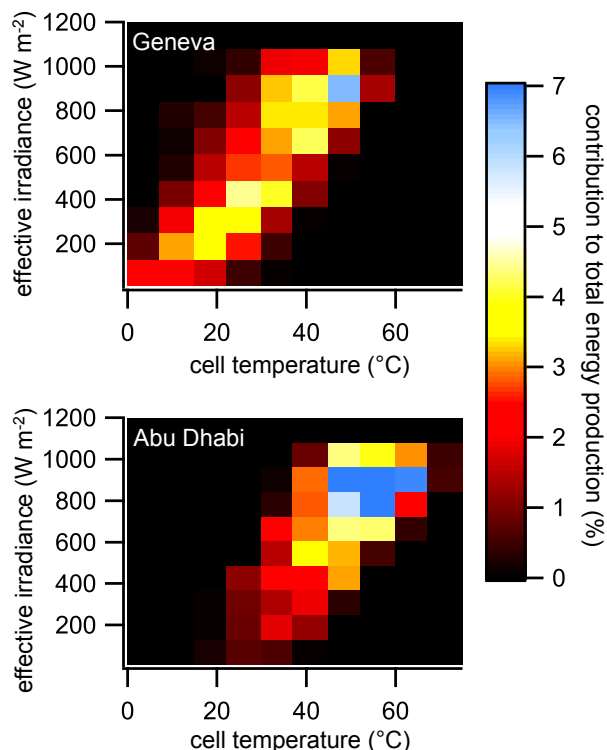
Fig. 8 Histograms of conditions at which energy is produced in Geneva and Abu Dhabi. The histograms are based on the weather data used for the calculation of the annual energy production.

Fig. 9 Efficiency of the p-BSF cell at 25 °C versus irradiance. The data in black correspond to the measured data; the grey data were calculated using equation (7) and assuming additional ohmic cell-to-module losses, R_{CTM}.
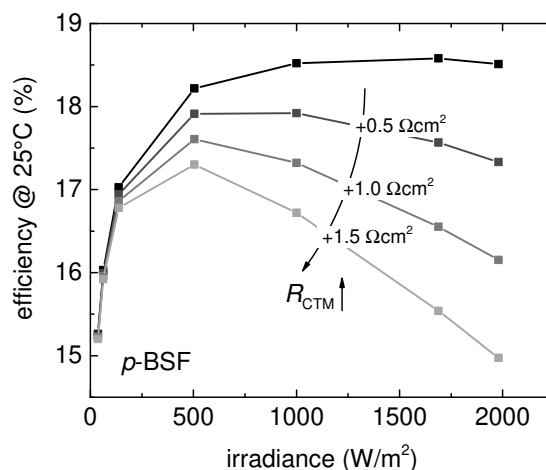
cell architectures and additional series resistance values, R_{CTM}, between $0.5 \, \Omega \, cm^2$ and $1.5 \, \Omega \, cm^2$. The annually produced energy, E_{yr}, was calculated as described in Section 2.2.3 for temperate (Geneva) and hot and sunny (Abu Dhabi) climate conditions. The resulting value of EPRP$_{cell}$ is thus the amount of energy in kWh that will be produced by one nominal kW of solar cells and assuming different R_{CTM}. Due to the non-linearity of the n-SHJ cell, its P_{MPP} at STC is reduced compared to what would be expected from its TC derived between 50 °C and 75 °C (c.f. Section 3.2). For a fair comparison, we therefore used the extrapolated value of $P_{MPP}^{STC,cell}$ as the divisor (the uncorrected data is about $1 \, \%_{abs}$ higher). It can be seen that in the temperate climate, all solar cell architectures feature a very similar EPRP$_{cell}$. However, the n-SHJ architecture suffers slightly less from the additional series resistance. In the hot climate, the differences between the technologies become more pronounced. Here, the n-SHJ technology benefits from its better TC$_{P_{MPP}}$. One kW of cells produces $2 \, \%$ more energy in comparison with the p-BSF architecture. The benefit increases further with the assumption of ohmic cell-to-module losses up to $3 \, \%$ at R_{CTM} of $1.5 \, \Omega \, cm^2$. Note, however, that a realistic value for R_{CTM} would be below $1 \, \Omega \, cm^2$, as discussed in Section 3.4. Limiting R_{CTM} to values between $0.5 \, \Omega \, cm^2$ and $1 \, \Omega \, cm^2$ allows us to compare the four technologies currently on the market (p-BSF, p-PERC, adv. n-PERT, n-SHJ), as shown in Fig. 7 on the right. It can be seen that the differences between the cell architectures are small enough to be potentially outweighed by the additional R_{CTM} present in a module.

Furthermore, it is interesting to note that the slope of all curves

is steeper with the subtropical climate conditions, indicating that R_{CTM} is more detrimental to energy production performance in subtropical climates than in temperate climates. This is also partly associated with an increasing share of ohmic losses at higher temperatures as discussed in Section 3.4. However, the main driver behind this effect is that, in Abu Dhabi, a larger part of the energy is produced at higher irradiance, i.e., between $800 \, W \, m^{-2}$ and $1000 \, W \, m^{-2}$ (cf. the yield histogram shown in Fig. 8). At higher irradiance, the detrimental influence of R_{CTM} is also higher as can be seen in Fig. 9, in which the irradiance-dependant efficiency at 25 °C is shown for the p-BSF cell. In Geneva, a larger share of the energy is produced at irradiances below $800 \, W \, m^{-2}$ and as a consequence the detrimental effect of R_{CTM} is counterbalanced.

It is striking that under temperate climate conditions (here: Geneva), EPRP$_{cell}$ is the same for all architectures. If the area for a photovoltaic system is not a constraint, all architectures will produce the same amount of energy at a given system power. Under hot climate conditions, the n-SHJ architecture produces more energy per kW. Depending on the price per kW, n-SHJ is therefore better suited for applications in hot climates. The superior performance of the SHJ architecture under hot climate conditions was also experimentally shown by Abdallah *et al.* [68] based on data from an outdoor test facility.

Furthermore, for hot and sunny climates, a technology with very low series resistance, both on the cell and module level, should be chosen. However, in optimizing of modules for applications in hot and sunny climates, the energy gain due to thicker and thus less resistive cell interconnection ribbons may outweigh their additional costs. The awareness of these points enables the adequate choice of the solar cell and module technology for an accurate calculation of the levelized cost of electricity (LCOE).

4 Conclusions

We presented temperature- and irradiance-dependent $J(V)$ measurements of silicon solar cells featuring state-of-the-art device architectures and the derived temperature coefficients (TCs) of the $J(V)$ parameters. When comparing the TC of the power at the maximum power point ($\text{TC}_{P_{\text{MPP}}}$) with data from module data sheets, we found that the TCs of the open-circuit voltage and the short-circuit current density of modules and cells are similar but $\text{TC}_{P_{\text{MPP}}}$ of the modules is generally worse.

This difference can be explained assuming that there is additional series resistance, R_{CTM}, which is induced by cell interconnections in a module. The additional R_{CTM} leads to a worse TC of the fill factor and hence a worse $\text{TC}_{P_{\text{MPP}}}$. We developed an equation to calculate the $\text{TC}_{P_{\text{MPP}}}$ of a module when the $\text{TC}_{P_{\text{MPP}}}$ and $R_{\text{MPP}}^{25\,°C}$ of the cells as well as $R_{\text{CTM}}^{25\,°C}$ are known.

Furthermore, we calculated the annually produced energy for the different architectures for two climates. Comparing the results, we showed that R_{CTM} is more detrimental in hot and sunny climate conditions. A solar cell architecture featuring high internal resistance at the maximum power point ($R_{\text{MPP}} = V_{\text{MPP}}/J_{\text{MPP}}$) performs best under such conditions and is less prone to losses due to R_{CTM}. Candidates to fulfill this are solar cell architectures featuring passivating contacts and thus high operating voltages such as silicon heterojunction architectures, which are included in our analysis.

In summary, for the highest performance in hot and sunny climates, a high V_{OC} on the cell level and low ohmic cell interconnections on the module level are essential.

References

1 D. B. Needleman, J. R. Poindexter, R. C. Kurchin, I. M. Peters, G. Wilson and T. Buonassisi, *Energy Environ. Sci.*, 2016, **9**, 2122–2129.

2 N. S. Lewis and D. G. Nocera, *Proceedings of the National Academy of Sciences of the United States of America*, 2006, **103**, 15729–35.

3 N. S. Lewis, *Science*, 2007, **315**, 798–801.

4 A. Louwen, W. G. J. H. M. van Sark, A. P. C. Faaij and R. E. I. Schropp, *Nature Communications*, 2016, **7**, 13728.

5 D. M. Powell, M. T. Winkler, H. J. Choi, C. B. Simmons, D. B. Needleman and T. Buonassisi, *Energy Environ. Sci.*, 2012, **5**, 5874 – 5883.

6 D. Yue, F. You and S. B. Darling, *Solar Energy*, 2014, **105**, 669–678.

7 J. Jean, P. R. Brown, R. L. Jaffe, T. Buonassisi and V. Bulovic, *Energy Environ. Sci.*, 2015, **8**, 1200–1219.

8 N. S. Lewis, *Science*, 2016, **351**, aad1920–1—–aad1920–9.

9 C. Battaglia, A. Cuevas and S. De Wolf, *Energy Environ. Sci.*, 2016, **9**, 1552–1576.

10 M. A. Green, *Nature Energy*, 2016, **1**, 15015.

11 P. Welter, *Photon International The Solar Power Magazine*, 2016, **6**, 10–13.

12 Agora Energiewende, *Current and Future Cost of Solar Photovoltaics*, 2015.

13 W. Cole, P. Kurup, M. Hand, D. Feldmann, B. Sigrin, E. Lantz, T. Stehly, C. Augustine, C. Turchi, P. O'Connor and C. Waldoch, *2016 Annual Technology Baseline*, Nrel (national renewable energy laboratory) technical report, 2016.

14 S. Szabó, M. Moner-Girona, I. Kougias, R. Bailis and K. Bódis, *Nature Energy*, 2016, **1**, 16140.

15 T. Kenning, *Lowest ever solar bids submitted in Abu Dhabi*, 2016, http://www.pv-tech.org/news/lowest-ever-solar-bids-submitted-in-abu-dhabi.

16 J. Parnell, *Masdar and FRV win 800MW Dubai tender*, 2016, http://www.pv-tech.org/news/masdar-and-frv-win-800mw-dubai-tender.

17 D. Ola, *Mexico issues draft guidelines for second power auction*, 2016, http://www.pv-tech.org/news/mexico-issues-draft-guidelines-for-second-power-auction.

18 L. Graves, *Dubai's Mohammed bin Rashid Al Maktoum Solar Park shatters world record again*, 2016, http://www.thenational.ae/business/energy/dubais-mohammed-bin-rashid-al-maktoum-solar-park-shatters-world-record-again.

19 S. B. Darling, F. You, T. Veselka and A. Velosa, *Energy & Environmental Science*, 2011, **4**, 3133.

20 M. Green, K. Emery and A. Blakers, *Electronics Letters*, 1981, **18**, 97–98.

21 J. Zhao, A. Wang, S. J. Robinson and M. A. Green, *Progress in Photovoltaics: Research and Applications*, 1994, **2**, 221–225.

22 M. A. Green, *Progress in Photovoltaics: Research and Applications*, 2003, **11**, 333–340.

23 M. A. Green, *Solar Cells*, 1982, **7**, 337–340.

24 M. Leilaeioun and Z. Holman, *2015 IEEE 42nd Photovoltaic Specialist Conference, PVSC 2015*, 2015.

25 M. Taguchi, E. Maruyama and M. Tanaka, *Japanese Journal of Applied Physics*, 2008, **47**, 814.

26 T. F. Schulze, L. Korte, E. Conrad, M. Schmidt and B. Rech, *Journal of Applied Physics*, 2010, **107**, 023711.

27 J. P. Seif, A. Descoeudres, M. Filipič, F. Smole, M. Topič, Z. C. Holman, S. De Wolf and C. Ballif, *Journal of Applied Physics*, 2014, **115**, 024502.

28 G. Nogay, J. P. Seif, Y. Riesen, A. Tomasi, Q. Jeangros, N. Wyrsch, F. J. Haug, S. De Wolf and C. Ballif, *IEEE Journal of Photovoltaics*, 2016, **6**, 1654–1662.

29 J. Schmidt, *Applied Physics Letters*, 2003, **82**, 2178–2180.

30 R. A. Sinton, A. L. Blum and J. S. Swirhun, *Solid State Phenomena*, 2013, **205-206**, 103–109.

31 J. P. Seif, G. Krishnamani, B. Demaurex, C. Ballif and S. De Wolf, *IEEE Journal of Photovoltaics*, 2015, **5**, 718–724.

32 T. Dullweber and J. Schmidt, *Ieee Journal of Photovoltaics*, 2016, **6**, 1–16.

33 J. Zhao and A. Wang, *Applied Physics Letters*, 2006, **88**, 242102.

34 S. De Wolf, A. Descoeudres, Z. C. Holman and C. Ballif, *Green*, 2012, **2**, 7–24.

35 *International Technology Roadmap for Photovoltaic (ITRPV)*, 2016.

36 R. Sinton and A. Cuevas, *Proceedings of the 16th European Photovoltaic Solar Energy Conference*, 2000, 1–4.

37 T. Dullweber, S. Gatz1, H. Hannebauer, T. Falcon, R. Hesse, J. Schmidt and R. Brendel, 26th European Photovoltaic Solar Energy Conference and Exhibition, 2011, pp. 811–816.

38 E. Cornagliotti, A. Uruena, B. Hallam, L. Tous, R. Russell, F. Duerinckx and J. Szlufcik, *Solar Energy Materials and Solar Cells*, 2015, **138**, 72–79.

39 L. Tous, M. Aleman, R. Russell, E. Cornagliotti, P. Choulat, A. Uruena, S. Singh, J. John, F. Duerinckx, J. Poortmans and R. Mertens, *Progress in Photovoltaics: Research and Applications*, 2015, **23**, 660–670.

40 M. Aleman, A. Uruena, P. Choulat, B. Hallam, C. Dang, R. Russell, F. Duerinckx, E. Cornagliotti and J. Szlufcik, 26th European Photovoltaic Solar Energy Conference and Exhibition, 2013, pp. 1689–1699.

41 E. Cornagliotti, A. Sharma, A. Uruena, M. Aleman, L. Tous, R. Russell, P. Choulat, J. Chen, J. John, F. Duerinckx, B. Dielissen, R. Görtzen, L. Black and J. Szlufcik, *The 6th World Conference on Photovoltaic Energy Conversion*, 2014, 543–544.

42 L. Tous, S. N. Granata, A. Rouhi, J.-F. Lerat, T. Emeraud, S. M. de Nicolas, T. M. Pletzer, R. Labie, M. Aleman, R. Russell, J. John, F. Duerinckx, J. Szlufcik, S. D. Wolf, C. Ballif, R. Mertens, J. Poortmans, S. De Wolf, C. Ballif and R. Mertens, *Energy Procedia*, 2014, **55**, 715–723.

43 A. Descoeudres, Z. C. Holman, L. Barraud, S. Morel, S. De Wolf and C. Ballif, *Photovoltaics, IEEE Journal of*, 2013, **3**, 83–89.

44 L. Tous, S. N. Granata, P. Choulat, T. Bearda, A. Michel, A. Uruena, E. Cornagliotti, M. Aleman, R. Gehlhaar, R. Russell, F. Duerinckx and J. Szlufcik, *Solar Energy Materials and Solar Cells*, 2015, **142**, 66–74.

45 A. Urueña, M. Aleman, E. Cornagliotti, A. Sharma, M. Haslinger, L. Tous, R. Russell, J. John, F. Duerinckx and J. Szlufcik, *Progress in Photovoltaics: Research and Applications*, 2016, **24**, 1149–1156.

46 J. Schmidt and R. A. Sinton, *Proceedings of the 3rd World Conference on Photovoltaic Energy Conversion*, 2003, 3001.

47 M. J. Kerr, A. Cuevas and R. A. Sinton, *Journal of Applied Physics*, 2002, **91**, 399–404.

48 *American Society of Heating, Refrigerating and Air Conditioning (ASHRAE), Inc., Atlanta, GA, USA www.ashrae.org*, 2001, https://energyplus.net/weather.

49 J. Stein, D. Riley and C. W. Hansen, *PV LIB Toolbox*, 2015, http://pvpmc.org.

50 S. Wang and D. MacDonald, *Journal of Applied Physics*, 2012, **112**, 113708.

51 T. Trupke, M. A. Green, P. Würfel, P. P. Altermatt, A. Wang, J. Zhao and R. Corkish, *Journal of Applied Physics*, 2003, **94**, 4930–4937.

52 H. T. Nguyen, S. C. Baker-Finch and D. MacDonald, *Applied Physics Letters*, 2014, **104**, 2014–2017.

53 J. P. Seif, D. Menda, A. Descoeudres, L. Barraud, O. Özdemir, C. Ballif and S. De Wolf, *Journal of Applied Physics*, 2016, **120**, 054501.

54 M. A. Green, *Solar Energy Materials and Solar Cells*, 2008, **92**, 1305–1310.

55 M. A. Green, A. W. Blakers and C. R. Osterwald, *Journal of Applied Physics*, 1985, **58**, 4402–4408.

56 K. Misiakos and D. Tsamakis, *Journal of Applied Physics*, 1993, **74**, 3293–3297.

57 A. Cuevas, *Energy Procedia*, 2014, **55**, 53–62.

58 D. C. Giancoli, *Physics: Principles with Applications*, Prentice Hall, 4th edn, 1995.

59 S. Braun, G. Hahn, R. Nissler, C. Pönisch and D. Habermann, *The multi-busbar design: An overview (oral presentation)*, 2013, http://www.metallizationworkshop.eu/fileadmin/metallizationworkshop/docs/presentations2013/Session{_}VI{_}Braun.pdf.

60 S. Braun, R. Nissler, C. Ebert, D. Habermann and G. Hahn, *Ieee Journal of Photovoltaics*, 2014, **4**, 148–153.

61 R. Witteck, D. Hinken, H. Schulte-Huxel, M. R. Vogt, J. Muller, S. Blankemeyer, M. Kontges, K. Bothe and R. Brendel, *IEEE Journal of Photovoltaics*, 2016, **6**, 432–439.

62 S. Braun, G. Hahn, R. Nissler, C. Pönisch and D. Habermann, *Energy Procedia*, 2013, **43**, 86–92.

63 J. Levrat, K. Thomas, A. Faes, J. Champliaud, C. Allebé, N. Badel, L. Barraud, F. Debrot, A. Descoeudres, A. Lachowicz, M. Kiaee, M. Despeisse and C. Ballif, Photovoltaic Specialist Conference (PVSC), 2015 IEEE 42nd, 2015, pp. 2–4.

64 J. Walter, M. Tranitz, M. Volk, C. Ebert and U. Eitner, *Energy Procedia*, 2014, **55**, 380–388.

65 International Standard, *IEC 61724 - Photovoltaic system performance monitoring - Guidelines for measurement, data exchange and analysis*, 1998.

66 B. Marion, J. Adelstein, K. Boyle, H. Hayden, B. Hammond, T. Fletcher, B. Canada, D. Narang, A. Kimber, L. Mitchell, G. Rich and T. Townsend, *31st IEEE PVSC*, 2005, 1601–1606.

67 D. Rose, O. Koehler, B. Bourne, D. Kavulak and L. Nelson, 25th European Photovoltaic Solar Energy Conference and Exhibition / 5th World Conference on Photovoltaic Energy Conversion - Valencia, 2010, pp. 6–10.

68 A. Abdallah, D. Martinez, B. Figgis and O. El Daif, *Renewable Energy*, 2016, **97**, 860–865.